metals

MDPI

Article

Influence of Aluminum Content on the Microstructure, Mechanical Properties, and Hot Deformation Behavior of Mg-Al-Zn Alloys

Marie Moses *, Madlen Ullmann and Ulrich Prahl

Institute of Metal Forming, Technische Universität Bergakademie Freiberg, Bernhard-von-Cotta-Straße 4, 09599 Freiberg, Germany; madlen.ullmann@imf.tu-freiberg.de (M.U.); ulrich.prahl@imf.tu-freiberg.de (U.P.)
* Correspondence: marie_moses@outlook.de

Abstract: This study compares AZ91 with AZ31 to investigate the influence of a higher Al content on the resulting microstructure, mechanical properties, and hot deformation behavior. While AZ31 exhibits a globular structure after casting, AZ91 shows a fully developed dendritic structure due to the promotion of dendrites. A heat treatment helped to homogenize AZ31, dissolved a large part of the Mg-Al precipitations in AZ91, and formed globular grains in AZ91. Due to the impact of Al on constitutional supercooling, AZ91 exhibits smaller grains than AZ31. Because of the strengthening of the solid solution, AZ91 also exhibits higher strength and hardness compared to AZ31. Cylindric compression tests of the heat-treated samples were conducted at different temperatures (300–400 °C) and strain rates ($0.1 \times 10\ s^{-1}$). The main dynamic recrystallization (DRX) mechanisms in AZ31 and AZ91 are twinning-induced DRX and discontinuous DRX. It was detected that $Mg_{17}Al_{12}$ precipitates at the grain boundaries in AZ91, which influences the grain size through pinning. Similar results could be conducted in rolling trials. Although both alloys have similar grain sizes after rolling, AZ91 exhibits higher strengths, while AZ31 shows higher ductility. This can be explained by the solid solution strengthening in AZ91 and less brittle $Mg_{17}Al_{12}$ precipitations in AZ31.

Keywords: AZ31; AZ91; microstructure; mechanical properties; flow curve; magnesium alloy; lightweight

Citation: Moses, M.; Ullmann, M.; Prahl, U. Influence of Aluminum Content on the Microstructure, Mechanical Properties, and Hot Deformation Behavior of Mg-Al-Zn Alloys. *Metals* **2023**, *13*, 1599. https://doi.org/10.3390/met13091599

Academic Editor: Ruizhi Wu

Received: 19 August 2023
Revised: 9 September 2023
Accepted: 13 September 2023
Published: 15 September 2023

1. Introduction

The use of magnesium alloys in the automotive industry is particularly interesting because of their lower density compared to other metallic materials and high specific strength. There are various other fields of application for magnesium alloys: aerospace, automotive, medical, electronic, sports, and defense technology [1–3]. Magnesium alloys can be divided into two categories: cast and wrought alloys. AZ91 is a very common example of a cast magnesium alloy, while AZ31 is a very popular wrought magnesium alloy. Both alloys contain 9 resp. 3 wt.% aluminum, and 1 wt.% zinc. Aluminum plays a key role in both magnesium alloys.

A higher Al content helps to improve the castability due to a larger solidification interval (compare 180 K for AZ91 and 130 K for AZ31 [4]). During solidification, the primary Mg matrix (α-Mg) solidifies first in the temperature range of 650–600 °C. Later, the eutectic reaction (Mg-$Mg_{17}Al_{12}$) occurs below 437 °C at the grain boundaries [5]. Under equilibrium cooling conditions, the eutectic phase $Mg_{17}Al_{12}$ is expected to appear in Mg-Al alloys with an Al content of approximately 13 wt.%. But, already, Mg alloys containing more than 2 wt.% Al show the secondary phase $Mg_{17}Al_{12}$ (eutectic phase) for non-equilibrium cooling conditions. The resulting size, shape, and distribution of the secondary phase have an impact on the ductility and creep resistance of the alloy. It can form in different morphologies depending on the solidification rate and the Al resp. Zn content [6]: fully or partially divorced eutectic [7]. Aluminum also influences the grain structure that forms.

Dahle et al. describe that a low Al content determines a globular structure after casting, but a higher Al content promotes the formation of a dendritic structure after casting [5]. During solidification, Al also has an impact on constitutional supercooling. This affects the growth restriction rate and, therefore, the impact on grain refinement [8]. By suppressing columnar grains and promoting narrower columnar grains with increasing Al content in pure Mg, Al influences the size of the resulting grains [8]. This means that the addition of Al can be used as a grain refinement method.

The Al content also influences the choice of heat treatment. For the AZ31 alloy, temperatures of 400 °C and holding times of approximately 12 h are generally sufficient to dissolve the precipitates of $Mg_{17}Al_{12}$ [9,10]. Their amount is reduced as a result of the lower Al content in the alloy, and their characteristic is usually fine and easier to dissolve. In the case of the AZ91 alloy, elevated temperatures (415 °C) and longer holding times (24 h) are recommended to dissolve the secondary phase [11–13]. The fully developed dendritic structure of the AZ91 alloy transforms into a globular structure after heat treatment [13]. It might be of interest to investigate whether the grain refinement effect is still visible after heat treatment in an AZ91 alloy compared to AZ31, though longer holding times and higher temperatures are recommended for the heat treatment to dissolve the higher amount of $Mg_{17}Al_{12}$ precipitations.

Although magnesium may tend to recover due to its high stacking fault energy, dynamic recrystallization (DRX) prevails due to the few slip systems available [14]. The nucleation of recrystallized grains occurs preferentially at existing high-angle grain boundaries. Furthermore, dynamic recrystallization can be initiated in twins, deformation inhomogeneities, such as deformation and shear bands, precipitations, or particles, as well as areas close to grain boundaries [15,16]. After a strong hardening, a new microstructure can be formed without the migration of a large-angle grain boundary; this process is understood as in situ or continuous dynamic recrystallization (CDRX). According to this, CDRX resembles a recovery process in which dislocations are consumed by small-angle grain boundaries, leading to the formation of new grains with high-angle grain boundaries [17]. The discontinuous dynamic recrystallization (DDRX) is characterized by the migration of a high-angle grain boundary. The form of a necklace structure is typical here [18]. In addition, grain boundary serration and bulging are an indication for DDRX [19]. Twin-induced dynamic recrystallization (TDRX) is often found in coarse-grained material, such as homogenized material [20,21]. Additionally, TDRX also occurs predominantly at lower degrees of deformation. It is reported that twinning is suppressed with an increasing Al content in Mg-Al-Zn alloys [22,23]. The bulging mechanism is characterized by the local movement of grain boundaries and occurs only in magnesium alloys at elevated temperatures and when the dislocation arrangement is favorable [20]. The particle-stimulated nucleation (PSN) is common in magnesium alloys containing rare-earth elements and leads to weaker texture formation, as the particles, which act as nucleation sites, form grains with a more random orientation [24]. Depending on the size, distribution, and proportion of the particles, they can support or suppress recrystallization [25]. The so-called pinning effect of $Mg_{17}Al_{12}$ precipitates was also described in Mg-Al-Zn alloys with an increased Al content. The size and number of precipitates are hereby decisive in terms of the influence on the resulting dynamically recrystallized grain size and the degree of dynamic recrystallization [21,26].

Not only can the Al content affect the DRX mechanism during hot deformation, but also a finer grain size before hot deformation [16,27]. In contrast, other publications show that the initial microstructure does not play a role [28]. Therefore, it is of particular interest to investigate the influence of grain refinement during solidification and heat treatment on hot deformation behavior. This study attempts to induce a finer grain size in AZ91 than in AZ31 after casting through the influence of the alloying element Al. This research is part of broader research exploring grain refinement methods and their effect and inheritance before, during, and after deformation. The AZ31 alloy is compared with the AZ91 in terms of its deformation behavior, with the initial condition before deformation (heat-treated state) being appropriately matched to the alloy (different temperatures and holding times

due to the amount of Al). Further, this study investigates whether a variation in alloying content influences the microstructure, texture, and mechanical properties during annealing and hot deformation.

2. Materials and Methods

The AZ31 and AZ91 ingots were melted and cast at 750 °C, resp., 720 °C (different temperatures due to the solidification interval) in dies with a diameter of 16 mm and a length of 250 mm. The steel dies were smoothened with boron nitride and graphite and preheated to 450 °C. Table 1 shows the chemical composition of the cast samples compared to the standard. AZ91 shows a slightly higher Al content compared to the standard.

Table 1. Chemical composition of the AZ31 and AZ91 samples compared to the standard in wt.%.

Alloy	Al	Zn	Mn	Balance	Mg
AZ31	2.8	0.7	0.3	0.0	96.2
AZ31 standard (DIN EN 12438) [29]	2.5–3.5	0.6–1.4	0.2–1.0	-	-
AZ91	9.6	0.6	0.2	0.0	89.6
AZ91 standard (ASTM B93) [30]	8.5–9.5	0.45–0.9	0.17–0.4	-	-

Heat treatment was carried out in an air radiation furnace. The following heat treatments were chosen according to the literature: 400 °C, 12 h for AZ31 [9,10], and 415 °C, 24 h for AZ91 [11–13]. After heat treatment, the samples were rapidly cooled in water.

Cylindric compression samples (10 mm in diameter, 18 mm in height) were milled from these heat-treated samples. Hot compression tests were conducted in the Warmumformsimulator (WUMSI) at temperatures of 300, 350, and 400 °C and strain rates of 0.1, 1, and 10 s^{-1} to an equivalent logarithmic strain of 1. After heating the samples in an air radiation furnace for 15 min at elevated temperatures, they were deformed and then water quenched. Graphite was used as a lubricant. The recorded flow curves were corrected for temperature and friction.

Groove rolling tests were performed on a three-high-standing rolling mill at the Institute of Metal Forming at TU Bergakademie Freiberg. Oval rolling samples with a height of 9.2 mm and a width of 20 mm were milled from the cast and heat-treated samples. Before rolling, the samples were heated to an elevated temperature (350 °C for AZ31 and 300 °C for AZ91 due to cracking during rolling at higher temperatures) in an air radiation furnace. Within five rolling steps, using a square-oval calibration, the rolling samples were deformed to a final diameter of 9.8 mm. The rolling speed was 1.5 m/s and the summed logarithmic strain reached 0.65.

Samples of the AZ31 and AZ91 alloys in the cast, heat-treated, compressed, and rolled state were embedded in the longitudinal section, ground with SiC abrasive paper, and polished with OP-chem and MD-Chem OPS 300 polishing cloths. The cast and heat-treated samples were etched using picric acid (5 mL glacial acetic acid, 6 g picric acid, 10 mL distilled water, and 100 mL ethanol) for 10–20 s. The deformed samples were etched using nitric acid (20 mL glacial acetic acid, 1 mL nitric acid, 20 mL distilled water, and 60 mL ethanol) for 45–50 s. Optical characterization was performed with the digital microscope VHX-6000 (Keyence Corporation, Osaka, Japan). The grain sizes were measured using the linear intercept method.

Furthermore, the scanning electron microscope Jeol JSM 7800 F (Tokyo, Japan) was used to take SE pictures and measure alloy composition using energy-dispersive X-ray spectroscopy (EDX). In addition, texture analysis was carried out by electron backscattering diffraction (EBSD) using an accelerating voltage of 20 kV and a step size depending on grain size (0.1–2 µm). The EBSD data were analyzed using the MTEX MATLAB toolbox [31].

Quasi-static tensile tests of the heat-treated and rolled samples were conducted at the AG100 at room temperature. The testing speed reached 0.625 mm/min. The sample form was B (according to standard DIN EN 50125) [32] with a measurement diameter of

5 mm and a measurement length of 25 mm. Vickers HV 10 hardness measurements were carried out on cast, heat-treated, and rolled samples using the ZHU250 (Zwick/Roell, Ulm, Germany).

3. Results and Discussion

3.1. As-Cast and Heat-Treated State

Figure 1 shows the microstructure of the cast (a) AZ31 and (b) AZ91 magnesium alloy. A globular structure can be seen for the AZ31, while the AZ91 alloy exhibits a fully developed dendritic structure. This can be mainly explained by the higher Al content, which promotes the formation of dendrite arms [5].

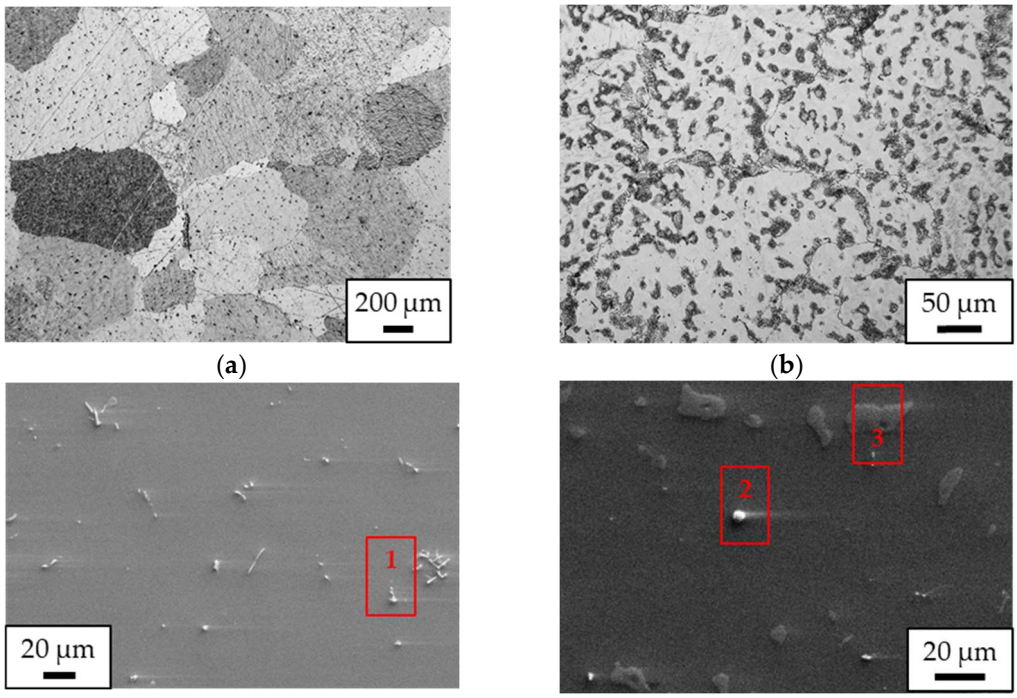

wt.%	Mg	Al	Zn	Mn	Si
1	26.8	29.0	0.9	42.9	-
2	6.7	41.4	0.3	49.8	1.8
3	60.6	35.7	3.6	0.0	0.0

(e)

Figure 1. Microstructure of the cast magnesium alloy (**a**) AZ31 and (**b**) AZ91. SEM images of the cast magnesium alloy (**c**) AZ31 and (**d**) AZ91 with EDX measurements in (**e**).

As mentioned before, Mg-Al alloys that do not solidify under equilibria conditions are expected to form the secondary eutectic phase $Mg_{17}Al_{12}$ when having more than 2 wt.% Al [5]. Although this phase could not be clearly detected in AZ31, the precipitate could be measured in AZ91 (see Figure 1d, point (3)). Furthermore, the Al_8Mn_5 precipitates are probably visible in both alloys (see Figure 1c,d, points (1) and (2)) [33]. Due to the higher Al content, AZ91 exhibits a higher amount of the secondary eutectic phase, which develops between the dendrite arms. The precipitations are evenly distributed. While the Al_8Mn_5 precipitates have a rather round, sometimes rod-like shape, the $Mg_{17}Al_{12}$ phase is extensive and significantly longer and larger. The size of an Al-Mn-based precipitate is approximately 2–5 µm and that of the Mg-Al precipitation is approximately 5–15 µm. The Al content in the magnesium matrix of AZ91 is also higher compared to AZ31 (4 wt.% compared to 2 wt.%).

Due to heat treatment, the grain structure of AZ91 transforms into a globular grain structure (see Figure 2). Furthermore, the SEM images reveal that the $Mg_{17}Al_{12}$ precipitates could be mainly dissolved in the matrix. This is supported by the fact that the Al content in the magnesium matrix of the heat-treated AZ91 sample is higher than in the cast AZ91 sample (9 wt.% compared to 4 wt.%). The Al content of the AZ31 matrix is also increasing (4 wt.% compared to 2 wt.%). The Al_8Mn_5 precipitates, measured at points one and two in Figure 2 [33], are still visible in both alloys after heat treatment. They cannot dissolve [34], and their size remains the same.

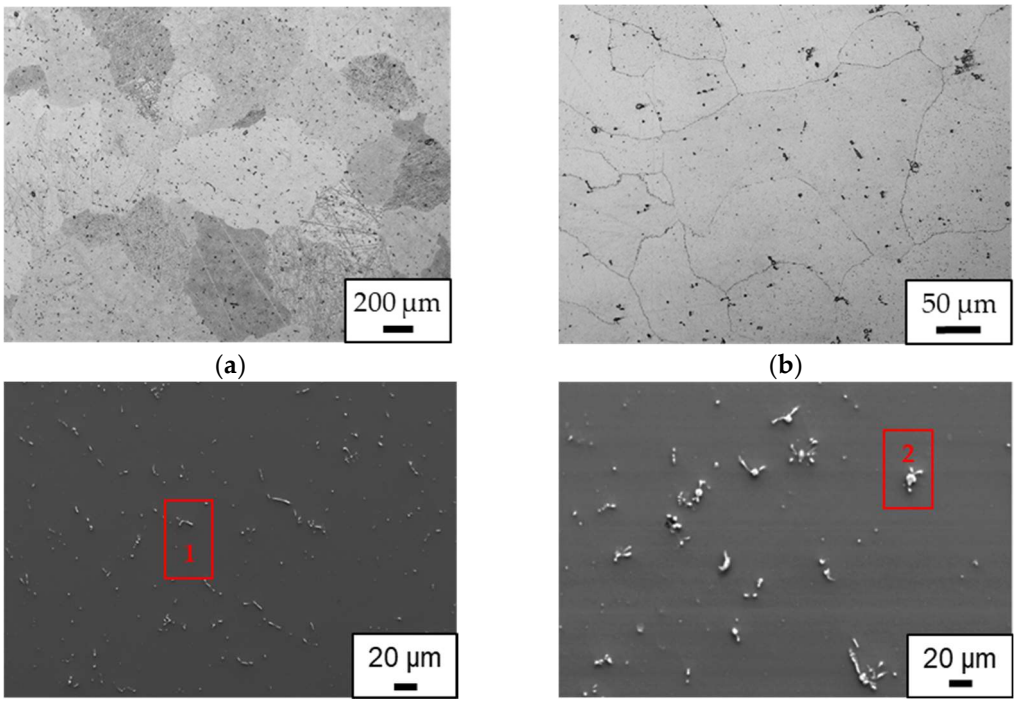

wt.%	Mg	Al	Zn	Mn	Si
1	53.1	24.8	3.3	16.6	1.4
2	21.2	32.4	3.9	41.5	1.0

(e)

Figure 2. Microstructure of the heat-treated magnesium alloy (**a**) AZ31 (400 °C, 12 h) and (**b**) AZ91 (415 °C, 24 h). SEM images of the heat-treated magnesium alloy (**c**) AZ31 and (**d**) AZ91 with EDX measurements in (**e**).

Finally, the EBSD maps of the cast and heat-treated samples were examined. Figure 3a,b shows whether AZ31 or AZ91 offers a preferred orientation because no color (red, blue, green) is represented in priority. This is also supported by the inverse pole figures shown in Figure 3c,d for AZ31 and AZ91, respectively. No clear orientation is present whether in the radial casting direction or longitudinal casting direction.

Figure 4 shows the grain size distribution of the cast and heat-treated AZ31 and AZ91. In general, the grain size is coarse because the material is poured and heat treated, but AZ91 exhibits in both, as-cast and heat-treated state, smaller grains than AZ31. This might be primarily due to the grain refining effect of the higher Al content and its impact on constitutional supercooling (in the case of the cast state). In the case of the heat-treated samples, a lower grain size of AZ91 could be due to inheritance effects, though a higher temperature and longer holding time were used to dissolve $Mg_{17}Al_{12}$ precipitations.

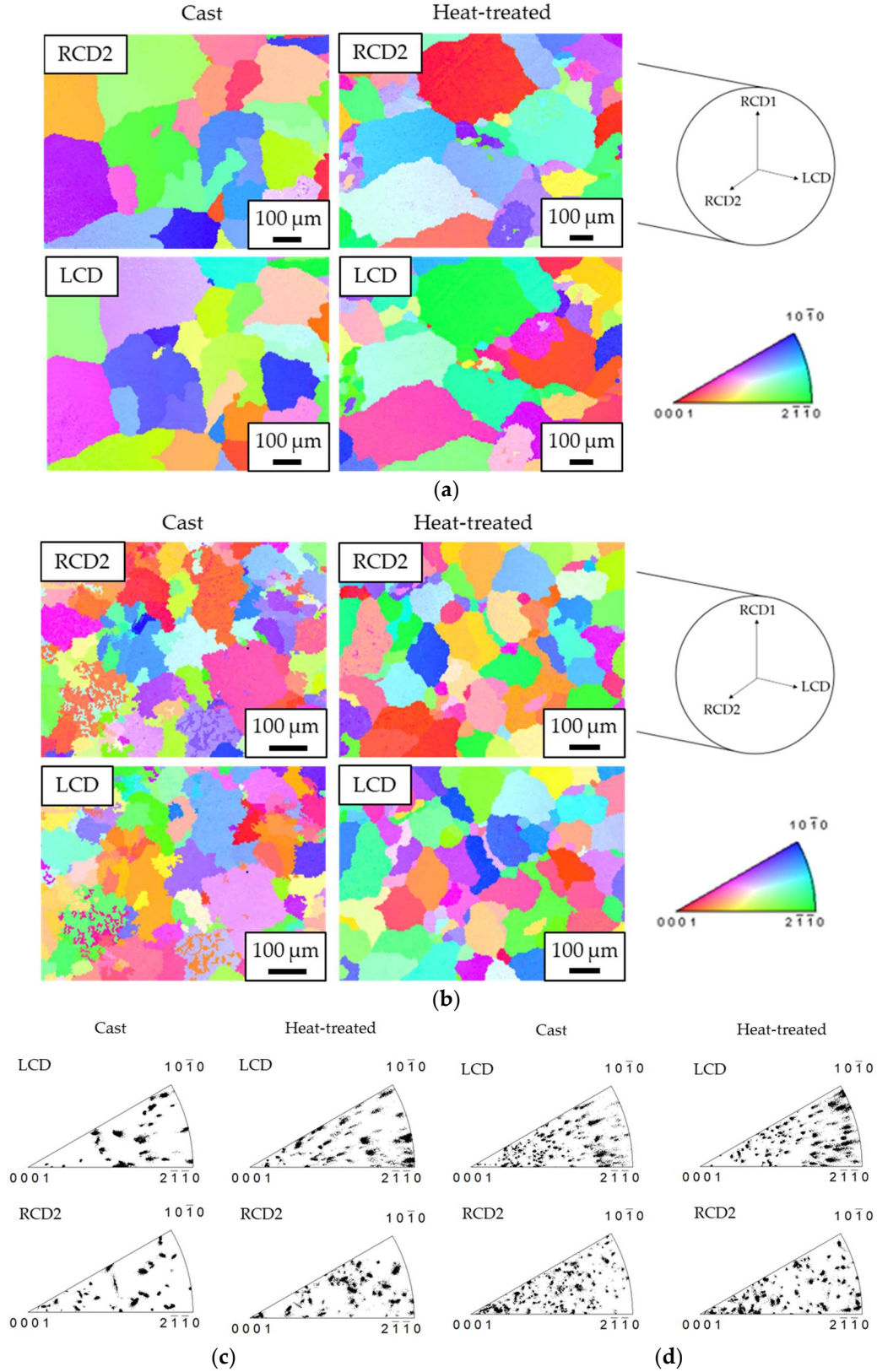

Figure 3. EBSD of the cast and heat-treated magnesium alloy (**a**) AZ31 and (**b**) AZ91 in radial casting direction 2 (RCD2) and longitudinal casting direction (LCD). Inverse pole figures of the cast and heat-treated magnesium alloy (**c**) AZ31 and (**d**) AZ91 in RCD2 and LCD.

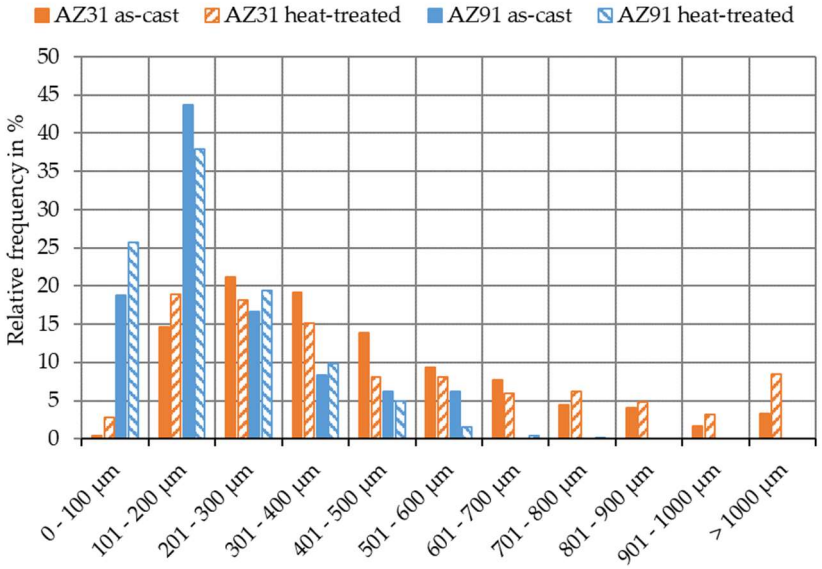

Figure 4. Grain size distribution of the heat-treated magnesium alloy AZ31 and AZ91 compared to the cast state.

The hardness values in Table 2, measured at room temperature (RT), show that the hardness of AZ91 significantly decreases after heat treatment. This is attributed to the dissolution of Al in the Mg matrix. In contrast to that, no clear trend could be determined in the case of AZ31, as the hardness drop is in the measurement error. AZ91 exhibits higher hardness values due to the higher amount of Al and its solid solution strengthening, as well as the grain refinement effect. It is already reported in the literature that the hardness increases with the Al content [35].

Table 2. Hardness values of the magnesium alloys AZ31 and AZ91 in cast and heat-treated state.

Hardness HV10 (RT)	As Cast	Heat-Treated
AZ31	49 ± 5	46 ± 2
AZ91	74 ± 2	61 ± 2

Table 3 shows the mechanical properties of the heat-treated alloys AZ31 and AZ91 conducted at room temperature. While AZ31 exhibits higher ductility, AZ91 shows higher strengths in the heat-treated state. This is mainly due to the higher Al content in AZ91 and the effect of Al on solid solution strengthening and grain size. In contrast to that, due to the lower Al content, AZ31 exhibits a higher stacking fault energy (SFE) [36], which might contribute to a higher ductility of the material.

Table 3. Mechanical properties of the alloys AZ31 and AZ91 in the heat-treated state at room temperature.

Mechanical Properties (RT)	Yield Strength (MPa)	Tensile Strength (MPa)	Elongation at Break (%)
AZ31	63 ± 7	192 ± 16	11 ± 1
AZ91	86 ± 4	229 ± 11	8 ± 1

The solidification rate of AZ91 in permanent mold casting is typically 10 K/s [37]. By examining the secondary dendrite arm spacing (*SDAS*) and calculating the solidification rate, a comparison between the investigation and the literature can be drawn. An *SDAS* of 33 µm was measured for AZ91. Using the equation

$$SDAS = 10.5\, t_f{}^{0.4}, \quad (1)$$

a local solidification time t_f of 17.5 s was calculated. Assuming a solidification interval T_s of 163 K for AZ91 [38], a solidification rate of 9.3 K/s was then calculated using the formula:

$$Solidification\ rate = \frac{\Delta T_s}{t_f}. \quad (2)$$

This shows that the solidification rate of the AZ91 alloy is a typical solidification rate for a material in permanent mold casting. The solidification rate of AZ31 could not be identified metallographically due to the globular structure.

However, the solidification rates of AZ31 and AZ91 during casting were additionally measured using a thermocouple placed in the middle of a steel die (see Figure 5). The solidification curves show a similar course though casting was carried out at different temperatures. The bend in the curves may be attributed to the solidification of the material (transition of liquid + Mg to Mg in the phase diagram). Due to the difference in the Al content, the change in the curve takes place at a lower temperature for AZ91 and affects the solidification rate strongly. However, the longer the time, the more the solidification rate of AZ31 is expected to be similar to that of AZ91.

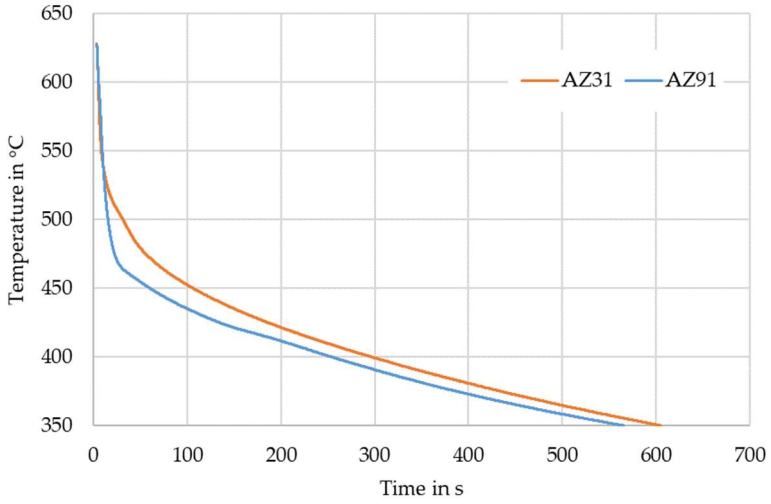

Figure 5. The solidification rate of AZ31 and AZ91.

All in all, a finer grain size was induced in the AZ91 alloy compared to the AZ31 alloy after casting due to the solute element Al and its influence on constitutional supercooling. The finer grain size is still present after heat treatment. A fully developed dendritic structure in the case of AZ91 after solidification could be formed into a globular structure after heat treatment. In addition, $Mg_{17}Al_{12}$ precipitations were dissolved during heat treatment, which resulted in a lower hardness after heat treatment for AZ91. In the case of the AZ31 alloy, a globular structure was already present after casting. No preferred orientation is present in both alloys. Due to solid solution strengthening, AZ91 exhibits higher strengths, while AZ31 shows a higher ductility in the heat-treated state.

3.2. Compressed State

Figure 6 shows the flow curves of the hot compressed alloys AZ31 and AZ91 after casting and heat treatment. The flow curves of AZ31 and AZ91 are characteristic flow curves for these magnesium alloys and correspond to the literature [14,39,40]. In the diagrams, a representative curve from each of the multiple trials is shown. The scatter of the curves is quite low with 5 MPa. As both alloys show flow curves with an increase and decrease in flow stress with increasing logarithmic strain, it is assumed that dynamic recrystallization is more dominant than dynamic recovery.

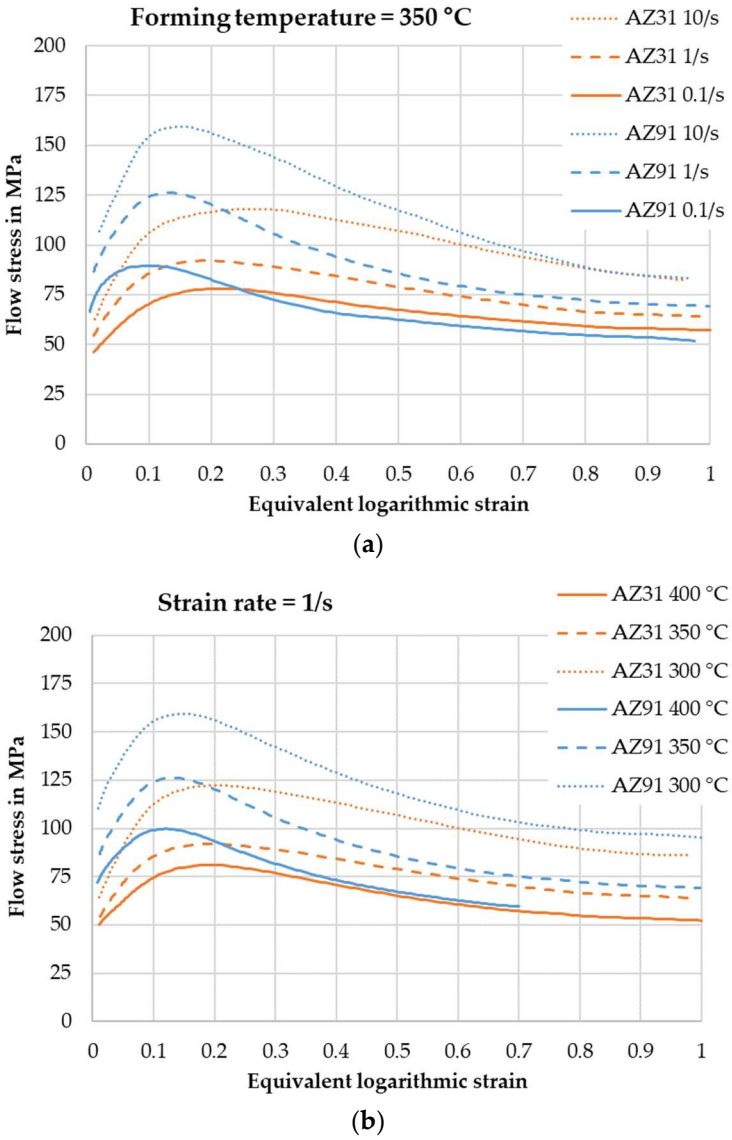

Figure 6. Flow curve of the AZ31 and AZ91 alloy at (**a**) a forming temperature of 350 °C and at (**b**) a strain rate of 1/s.

AZ91 often exhibits a steeper slope and decline than AZ31 at the same forming temperature and strain rate. It was already reported in the literature that Mg-Al alloys with a higher Al content tend to show higher peak flow stresses compared to Mg-Al alloys with a lower Al content due to the strengthening effect of the solute [35]. In addition, AZ91 exhibited a finer grain size before hot deformation, contributing to hardening. The maximum flow stresses of the AZ91 magnesium alloy are shifted to lower logarithmic strains and higher flow stresses compared to AZ31 at the same forming temperature and strain rate. This was also already reported in the literature for Mg-Al alloys with a higher Al content [19]. The flatter flow curves of AZ31 compared to AZ91 could be an indication that AZ31 has a higher tendency toward CDRX relative to AZ91, which might have a higher tendency toward DDRX. This may be attributed to a higher stacking fault energy (SFE) of AZ31 relative to AZ91 due to its lower Al content [19,36,40].

Figure 7 depicts the microstructure of the compressed AZ31 and AZ91 samples at a forming temperature of 350 °C, a strain rate of 1 s^{-1}, and a logarithmic strain of about 0.2. The black dots in the microstructure of AZ91 are probably Mg-Al precipitations that are precipitating during hot deformation. The SEM picture of the AZ91 alloy also reveals that the secondary phase precipitates (see Figure 7c,d) along the grain boundaries and inside the

grains. The precipitation of $Mg_{17}Al_{12}$ was not observed for AZ31. In both alloys, probably Al_8Mn_5 particles could be detected (an example of AZ91 is shown; see EDX measurement in Figure 7d). It is reported in the literature that Mg-Al-Zn alloys with higher Al content (e.g., AZ80) tend to show the initiation of DDRX at lower strains than Mg-Al-Zn alloys with a lower Al content (e.g., AZ31) [19]. Therefore, the AZ91 alloy is expected to show a higher amount of DRX grains compared to AZ31 at the logarithmic strain of 0.2. This can be observed in the microstructural pictures in Figure 7a,b. The newly formed grains are aligned along the original grain boundaries, indicating DDRX. In addition, the lower initial grain size of the AZ91 alloy probably contributes to a higher amount of DRX grains due to its effects on enhancing the nucleation rate. It was reported earlier that the initial microstructure influences the DRX proportion in an AZ31 alloy [41,42].

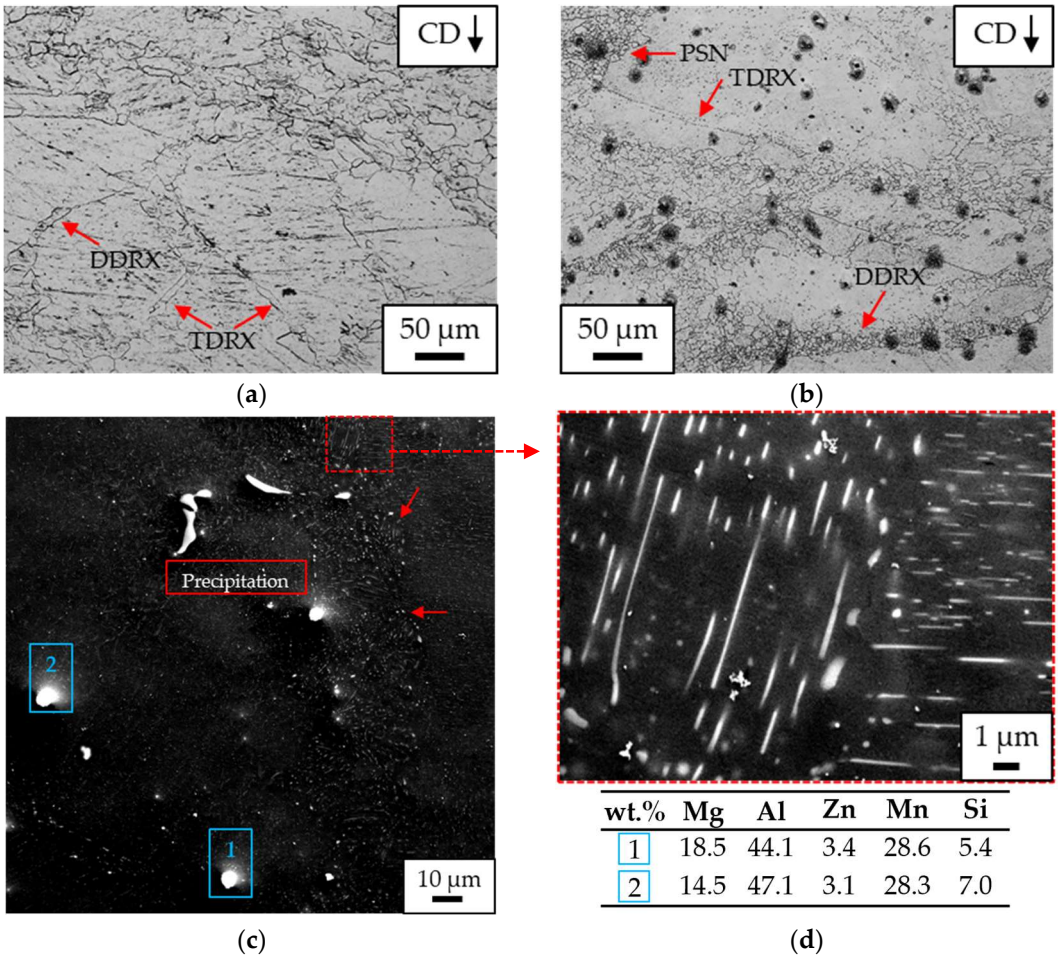

wt.%	Mg	Al	Zn	Mn	Si
1	18.5	44.1	3.4	28.6	5.4
2	14.5	47.1	3.1	28.3	7.0

Figure 7. Microstructure of the hot-deformed magnesium alloy (**a**) AZ31 and (**b**) AZ91 at a forming temperature of 350 °C, a strain rate of 1 s^{-1}, and a logarithmic strain of approximately 0.2. (**c**) SEM image of the AZ91 alloy showing the precipitation of $Mg_{17}Al_{12}$. (**d**) The magnification of precipitation inside the grains and the result of the EDX measurement shown in (**c**).

The mean DRX grain size is 10 ± 4 µm for AZ31 and 9 ± 3 µm for AZ91 at a forming temperature of 350 °C and a strain rate of 1 s^{-1}. It is reported that the higher the strain rate, the more comparable the DRX grain size will be between lower (AZ31) and higher (AZ80) Al-alloyed Mg-Al-Zn alloys [19]. This might explain the similar DRX grain size of both alloys.

As the secondary phase in AZ91 also precipitates along the grain boundaries, recrystallized grains and $Mg_{17}Al_{12}$ are often found together at the grain boundaries. Interestingly, the grain size near the precipitation is even smaller than farther away from the precipitation. Therefore, the precipitations might act as nucleation points (PSN) and have a pinning effect

on the recrystallized grains. Depending on their size, the precipitations can either promote (coarse particles) or hinder (fine dispersoids) recrystallization as they can act as nucleation sites or suppress the growth of DRX-grains [26]. Regarding the size of the precipitations in Figure 7, it is assumed that they might act as nucleation points for DRX.

In addition, twinning is observed as a deformation mechanism in both alloys. Due to a limited number of slip systems and an activation of twinning at a lower or equivalent stress, twinning is quite common in Mg alloys. Nevertheless, twinning is also influenced by the Al content. It is reported that the formation of twin lamellar structures is suppressed in Mg-Al-Zn alloys by increasing the Al content [22]. While double twins were more dominant in AZ31, extension twins without a lamellae structure nucleated in AZ91 [22]. Figure 8 presents the misorientation angle distribution of the magnesium alloys AZ31 and AZ91. The peak between 85 and 90 degrees may indicate $\{10\bar{1}2\}$ extension twins, while the peak at 35 degrees indicates $\{10\bar{1}1\}$-$[10\bar{1}2\}$ double twins. These double twins are generated due to $\{10\bar{1}2\}$ re-twinning inside a $\{10\bar{1}1\}$ compression twin and occur more frequently under compression when the stress direction is along the c-axis [43]. It seems to be that double twins are more dominant in AZ31 compared to AZ91, though both types are present in both alloys. It is known that the formation of $\{10\bar{1}2\}$ extension twins is much easier due to lower critical resolved shear stresses compared to $\{10\bar{1}1\}$ compression twins [23]. Nevertheless, the formation of $\{10\bar{1}1\}$ compression twins will be triggered due to basal texture formation under compression [21]. Then, $\{10\bar{1}1\}$-$[10\bar{1}2\}$ double twins will be formed to reduce the strain caused by $\{10\bar{1}1\}$ compression twins [21]. Further, it was reported that the presence of $Mg_{17}Al_{12}$ precipitations may lead to a lesser extent of twinning in AZ91 compared to AZ31 [23]. During hot deformation, $Mg_{17}Al_{12}$ precipitates as shown in Figure 7c,d. Depending on the size of the precipitation, they can act as barriers toward twin boundary migration and hinder the twin propagation rate [23].

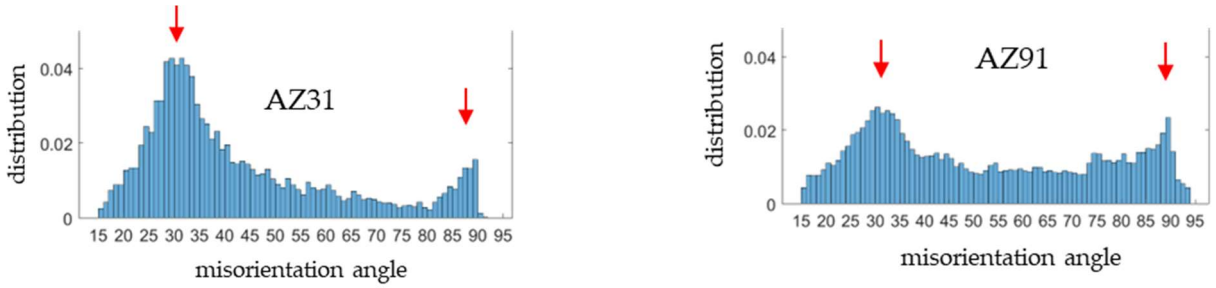

Figure 8. Misorientation angle distribution of (**a**) AZ31 and (**b**) AZ91 magnesium alloy at forming temperature of 350 °C and at a strain rate of 1/s.

In addition to DDRX, PSN, and TDRX, it is interesting to discuss the mechanism of CDRX during the deformation of AZ31 and AZ91. It was reported that the precipitation of $Mg_{17}Al_{12}$ in an AZ91 alloy hinders dislocation movement and, therefore, leads to dislocation pile-up near the precipitations and inside the grains, resulting in a promotion of the CDRX process [21]. This might be visible in the following EBSD picture of the AZ91 alloy during hot compression (see Figure 9b,d). For AZ31, it was reported that non-basal slip promotes CDRX in general, but DDRX is more dominant at higher temperatures compared to CDRX [18,39,44]. As the deformation took place at 350 °C, it is assumed that DDRX might be more dominant than CDRX in AZ31.

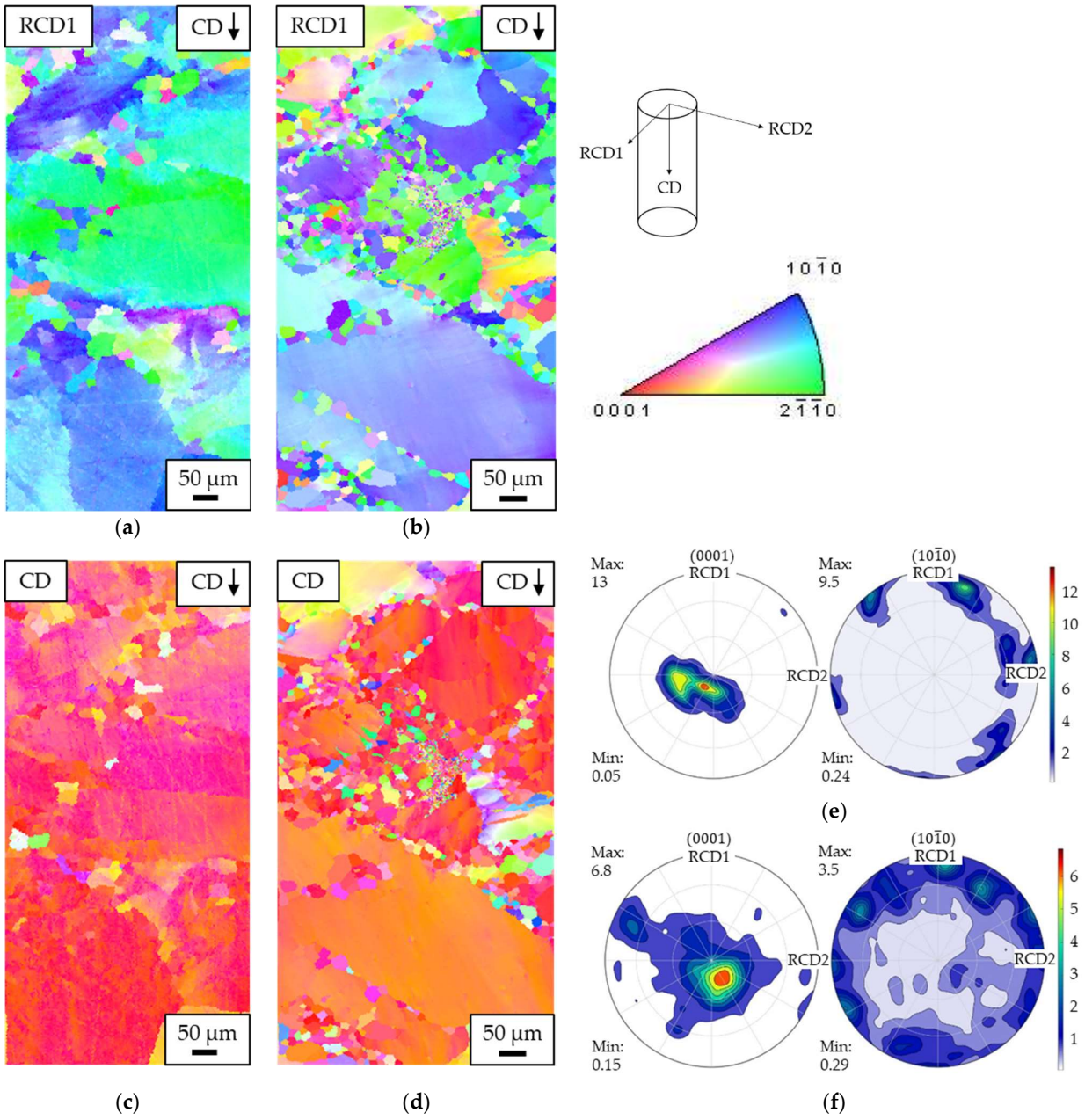

Figure 9. EBSD maps of the magnesium alloy AZ31 transverse to compression direction (CD) (**a**) in radial compression direction 1 (RCD1), (**c**) in CD and AZ91 transverse to CD (**b**) in RCD1, (**d**) in CD at a forming temperature of 350 °C, a strain rate of 1 s^{-1}, and a logarithmic strain of about 0.2. Pole figures showing (**e**) AZ31 and (**f**) AZ91 magnesium alloy.

The EBSD maps in Figure 9 show that a basal texture is present due to hot deformation. Since the grains in Figure 9a,b are primarily colored green or blue, this indicates that the hexagonal unit cells are aligned along the compression direction (CD). Therefore, the basal planes (marked red) are visible from the CD (see Figure 9c,d). The pole figures in Figure 9e,f also reveal that a basal texture is present. The intensity of the texture is lower in AZ91 compared to AZ31, probably due to the higher amount of DRX grains shown on the map, which promotes a less basal texture. It is reported in the literature that dynamically recrystallized grains in AZ91 contribute to a weaker texture, while the addition of Al limits the activation of prismatic slip, resulting in a strong texture for non-recrystallized grains [22].

To summarize this section, it can be stated that flow curves were obtained from the hot compression tests for AZ31 and AZ91. Both flow curves showed hardening and softening, a typical indication of dynamical recrystallization. By observing the microstructures at a forming temperature of 350 °C, a strain rate of 1 s^{-1}, and a logarithmic strain of about 0.2, it was found that $Mg_{17}Al_{12}$ precipitates at the grain boundaries in AZ91 and acts as nucleation sites for DRX. In both alloys, twinning was observed, acting as an initiation for DRX. In addition, DDRX is assumed to be dominant compared to CDRX in both alloys. A basal texture is present in both alloys after compression at a forming temperature of 350 °C, a strain rate of 1 s^{-1}, and a logarithmic strain of about 0.2. The texture intensity in AZ91 is lower, which was ascribed to more DRX grains in AZ91 with a random orientation. As the start of DRX is probably shifted to lower logarithmic strains due to the higher Al content, it is expected to see a higher amount of DRX grains in AZ91. In addition, the lower initial grain size in AZ91 may contribute to a higher amount of DRX grains.

3.3. Hot Deformation Behavior

To describe the dynamic recrystallization processes, the flow stress maxima, which depend on the strain rate and temperature, were obtained from the warm flow curves. This forms the basis for determining the activation energy Q for dynamic recrystallization using the logarithmic Arrhenius equation (see Equation (3)). This represents thermal activation during hot forming. Furthermore, the average model coefficients A (material constant), α (fitting parameter), and n (hardening exponent) can be graphically determined by using the slopes in the following diagrams and showing their relationships (see Figure 10). Furthermore, the Zener–Hollomon parameter Z, which summarizes the influence of the forming rate and thermal activation during hot forming, can be calculated using the formula:

$$Z = \dot{\varphi} e^{\left(\frac{Q}{RT}\right)} = A[\sinh(\alpha\, \sigma_{max})]^n. \quad (3)$$

$\dot{\varphi}$ represents the effective strain rate in s^{-1}, T the thermodynamic temperature, R the ideal gas constant (8.314 J(mol·K)), and σ_{max} the peak stresses. The following formulas result for AZ31 and AZ91:

$$\text{AZ31}\ \left(r^2 = 0.99\right):\ Z = \dot{\varphi} e^{\left(\frac{140{,}120}{RT}\right)} = 1.535{\cdot}10^{11}[sinh(0.010\, \sigma_{max})]^{7.965} \quad (4)$$

$$\text{AZ91}\ \left(r^2 = 0.99\right):\ Z = \dot{\varphi} e^{\left(\frac{146{,}780}{RT}\right)} = 5.638{\cdot}10^{11}[sinh(0.008\, \sigma_{max})]^{7.128}. \quad (5)$$

The activation energies between 105 and 185 kJ/mol are common for AZ alloys during hot deformation [45]. The calculated activation energy for AZ31 is 140 kJ/mol and, for AZ91, it is 147 kJ/mol. However, higher-alloyed AZ alloys show a higher activation energy for hot deformation compared to low-alloy AZ alloys [46,47]. In this present case, AZ91 exhibits only a slightly higher value than AZ31. All the values are above the self-diffusion value for magnesium (135 kJ/mol) [15].

Regarding the hardening parameter n, in the literature, it is said that there is a creep of dislocation climb present $n > 5$ [48,49]. Therefore, it is concluded that the dislocation climb creep is the dominant mechanism for both alloys since AZ31 and AZ91 exhibit higher values than 5 (7.965, resp., 7.128).

With the help of the so-called Kocks–Mecking plot, the development of the grain structure during deformation can be described. To evaluate the flow behavior, the strengthening rate (calculated slopes from the flow curves) was plotted against the flow stress. First, a strong and linear drop in hardening can be seen, which turns into an increase shortly before the maximum flow stress, which differs from the linear increase. This critical stress marks the beginning of dynamic recrystallization. A critical logarithmic strain for recrystallization can be assigned to that stress. Figure 11a shows the logarithmic strain for recrystallization in dependence on the Zener–Hollomon parameter, which has been determined mathematically. The critical degree decreases with increasing forming temperature (see Figure 11b)

and reduced strain rate, so the start of dynamic recrystallization shifts to lower logarithmic strains. The influence of forming temperature might be greater than the influence of the strain rate. AZ91 exhibits significantly lower logarithmic strains in dependence on Z and the forming temperature compared to AZ31.

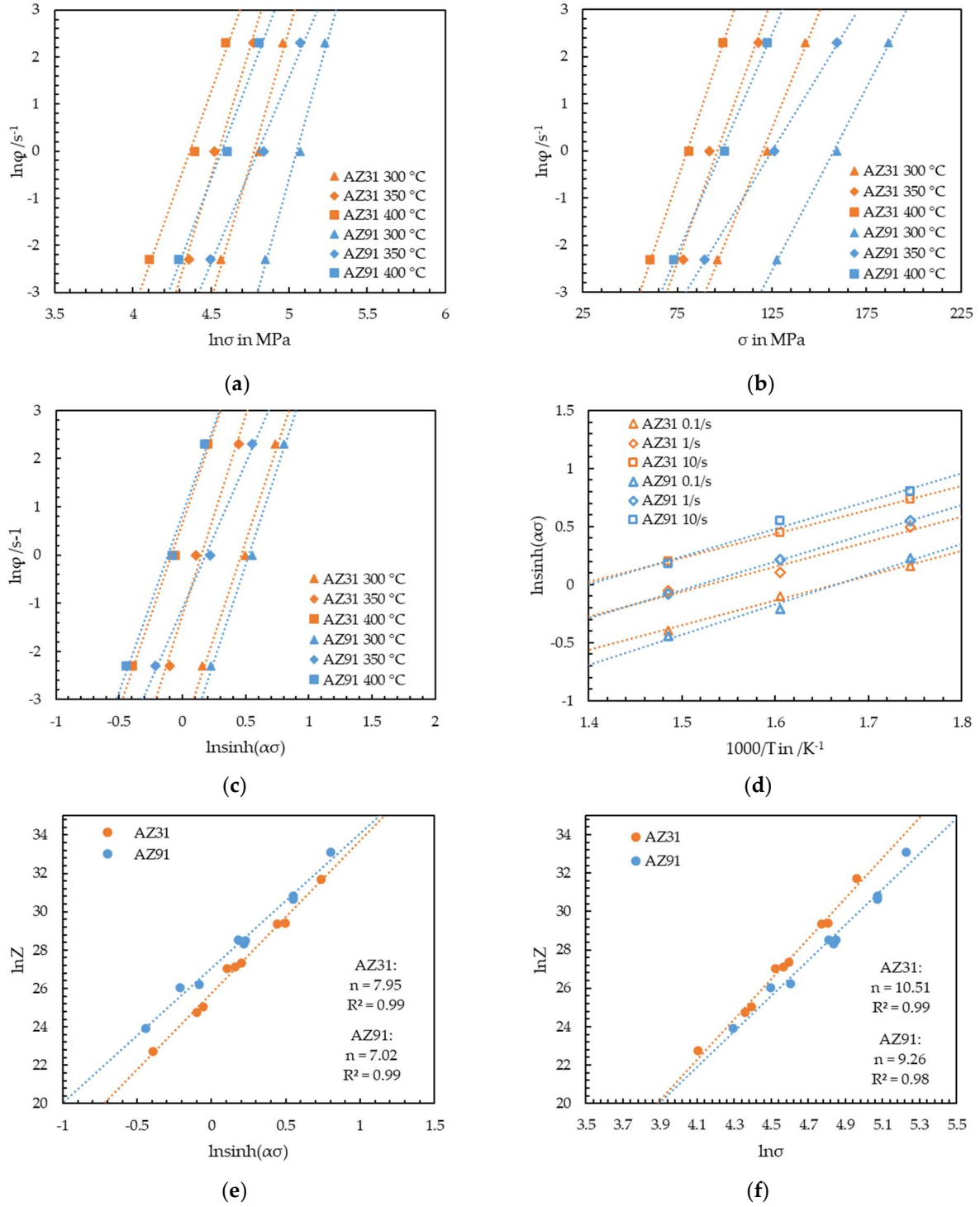

Figure 10. Relationship between ln$\dot{\varphi}$ and (**a**) ln(σ), (**b**) σ, and (**c**) lnsinh (ασ), the relationship between (**d**) lnsinh (ασ) and 1000/T, and the relationship between ln(Z) and (**e**) lnsinh (ασ) and (**f**) ln (σ) for AZ31 and AZ91 (cast, heat-treated, and hot-deformed).

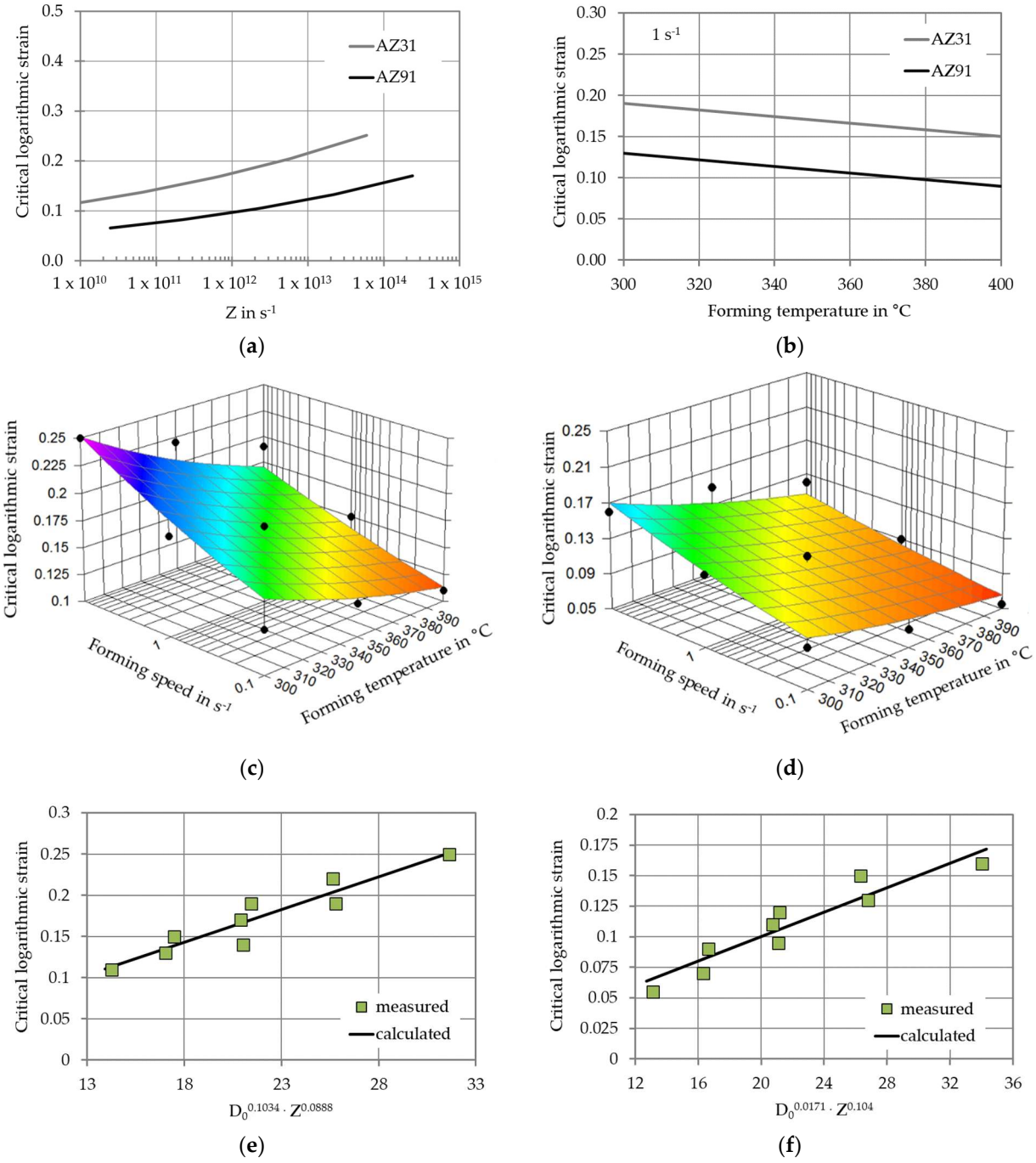

Figure 11. (**a**) Critical logarithmic strain in dependence on Zener–Hollomon parameter, (**b**) critical logarithmic strain in dependence of forming temperature for AZ31 and AZ91, (**c**) critical logarithmic strain in dependence of strain rate and temperature for AZ31, and (**d**) for AZ91, (**e**) comparison between measured and calculated results for AZ31 and (**f**) AZ91. Both alloys are cast, heat-treated, and hot-deformed.

Furthermore, the critical degree for all speeds and temperatures was graphically displayed from the experimental data and compared with the calculated results (see Figure 11c–f). For AZ31, the critical logarithmic strain for dynamic recrystallization for all speeds and temperatures lies between 0.11 and 0.25. However, AZ91 exhibits significantly lower values for the critical degree for all speeds and temperatures (0.055–0.16). Accordingly, the increased Al content contributes to the fact that the start of dynamic recrystallization is shifted to lower logarithmic strains.

The critical logarithmic strain for AZ31 and AZ91 can be summarized in the following equation:

$$\text{AZ31}\left(r^2 = 0.89\right): \varphi_c = a_1 \cdot {D_0}^{a_2} \cdot Z^{a_3} = 0.0079 \cdot {D_0}^{0.1034} \cdot Z^{0.0888} \quad (6)$$

$$\text{AZ91}\left(r^2 = 0.89\right): \varphi_c = a_1 \cdot {D_0}^{a_2} \cdot Z^{a_3} = 0.0050 \cdot {D_0}^{0.01715} \cdot Z^{0.1038}. \quad (7)$$

3.4. Rolled State

In the case of the AZ31 magnesium alloy, a good comparison can be made between the compression tests and the rolling tests. For the evaluation, however, it should be noted that the deformation rate in the rolling tests was significantly higher than 1 s^{-1}, as shown in Section 3.3. Therefore, in Figure 12, the EBSD maps of the first rolling pass (approximately 350 °C and about 15 s^{-1}) will be analyzed. With higher deformation rates, the start of dynamical recrystallization will be shifted to higher logarithmic strains. These are mostly achieved in the first pass so that recrystallization starts despite the increased strain rate. The discontinuous dynamical recrystallization (DDRX) mechanism could be observed after the first pass, probably due to higher strain rates [50,51]. In addition, the twinning mechanism was dominant due to the presence of a coarse initial grain structure, which is known to contribute to TDRX [20]. It is also reported that higher strain rates can contribute to twinning [19], which was the case during rolling. In total, the same mechanisms were observed that were already discussed with the compression sample at 350 °C and 1 s^{-1}.

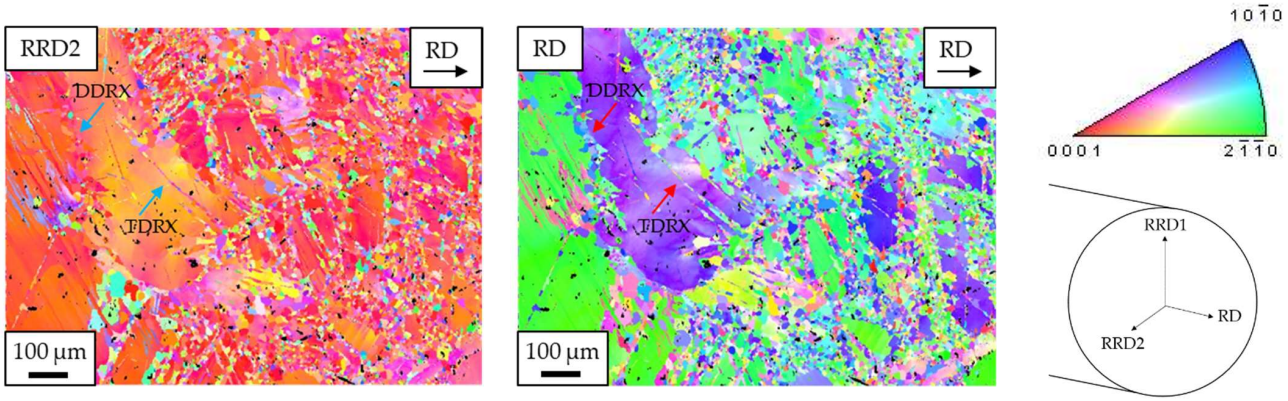

(**a**) (**b**)

Figure 12. EBSD maps of the rolled AZ31 magnesium alloy (first pass) transverse to RD, (**a**) in RRD2, and (**b**) in RD.

For the AZ91 magnesium alloy, it should be noted that the rolling temperature was reduced to 300 °C due to cracking during rolling at 350 °C. A reduced forming temperature contributes to the fact that the critical degree for DRX is shifted to higher logarithmic strains. However, this was already exceeded in the first rolling pass. Figure 13 shows the microstructure of the first pass of the AZ91 alloy. As a coarse grain structure is present, TDRX occurs. Furthermore, DDRX could be observed. Although DDRX is prevalent at higher forming temperatures, higher strain rates also contribute to this mechanism [50,51].

Moreover, the precipitation of the secondary phase can be detected. At higher temperatures, continuous precipitation occurs and the higher the forming temperature, the greater the amount of precipitation, but the less the effect of pinning [52]. At lower temperatures, discontinuous precipitation is present, and lower temperatures also lead to less precipitation of the secondary phase, but it enhances their pinning effect [14,52]. Pinning of the newly formed recrystallized grain boundaries restricts their growth and affects a lower DRX grain size. As precipitation takes place at the grain boundaries of the original grains, pinning and particle-stimulated nucleation is present there.

The microstructure of the magnesium alloys AZ31 and AZ91 after five passes of hot rolling is shown in Figure 14. AZ91 exhibits a lower grain size, which may be due to the lower rolling temperature used for AZ91. Additionally, the secondary phase $Mg_{17}Al_{12}$ precipitates at the grain boundaries during hot deformation (see Figure 14d). An EDX analysis reveals that the Al content in the matrix of AZ91 is slightly decreasing due to precipitation (8 wt.% compared to 9 wt.%). This was not observed for AZ31, as the Al content stays the same (4 wt.%). However, Al_8Mn_5 particles are present in both alloys.

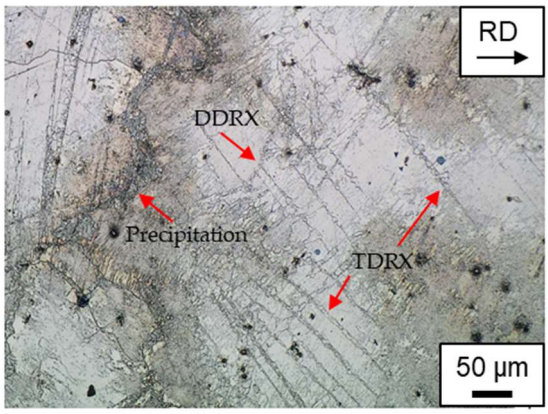

Figure 13. Microstructure of the AZ91 magnesium alloy after the first rolling pass, showing TDRX, DDRX, and precipitation.

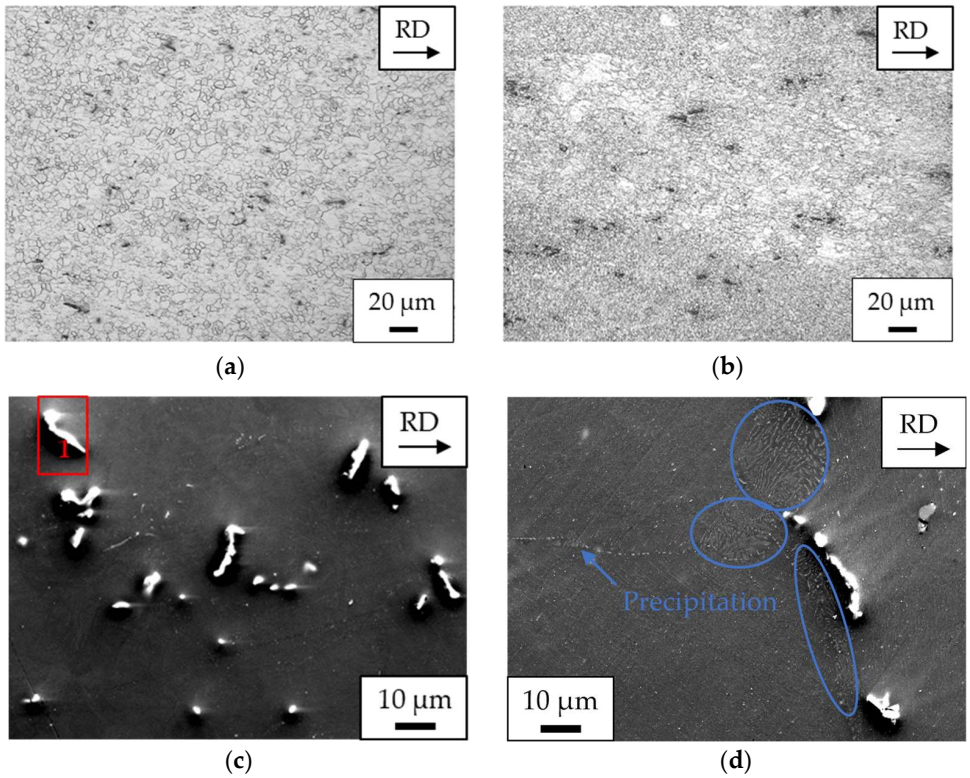

wt.%	Mg	Al	Zn	Mn	Si
1	43.6	32.4	1.1	20.8	2.2

(e)

Figure 14. Microstructure of the rolled (five passes) magnesium alloys (**a**) AZ31 and (**b**) AZ91. SEM images of the rolled (five passes) magnesium alloys (**c**) AZ31 and (**d**) AZ91; blue marked is precipitation of $Mg_{17}Al_{12}$. (**e**) EDX measurement. RD is the rolling direction.

Compared to the heat-treated state, the grain size of AZ31 and AZ91 could be significantly decreased during hot rolling. After five passes, the mean grain size of AZ31 is 5 ± 2 µm, while AZ91 has a mean grain size of 4 ± 1 µm.

The EBSD maps for both alloys are shown in Figure 15. A wire-rolling texture is present in which the hexagonal unit cells are horizontal and aligned transversely to the wire axis. The pole figures represent the intensity of the texture. AZ91 exhibits a lower texture intensity than AZ31. On the one hand, it may be because a lower rolling temperature was used for AZ91 and after the fifth pass there were still many randomly oriented, newly formed grains. On the other hand, the secondary phase precipitates during hot rolling, which promotes the formation of randomly oriented grains [17].

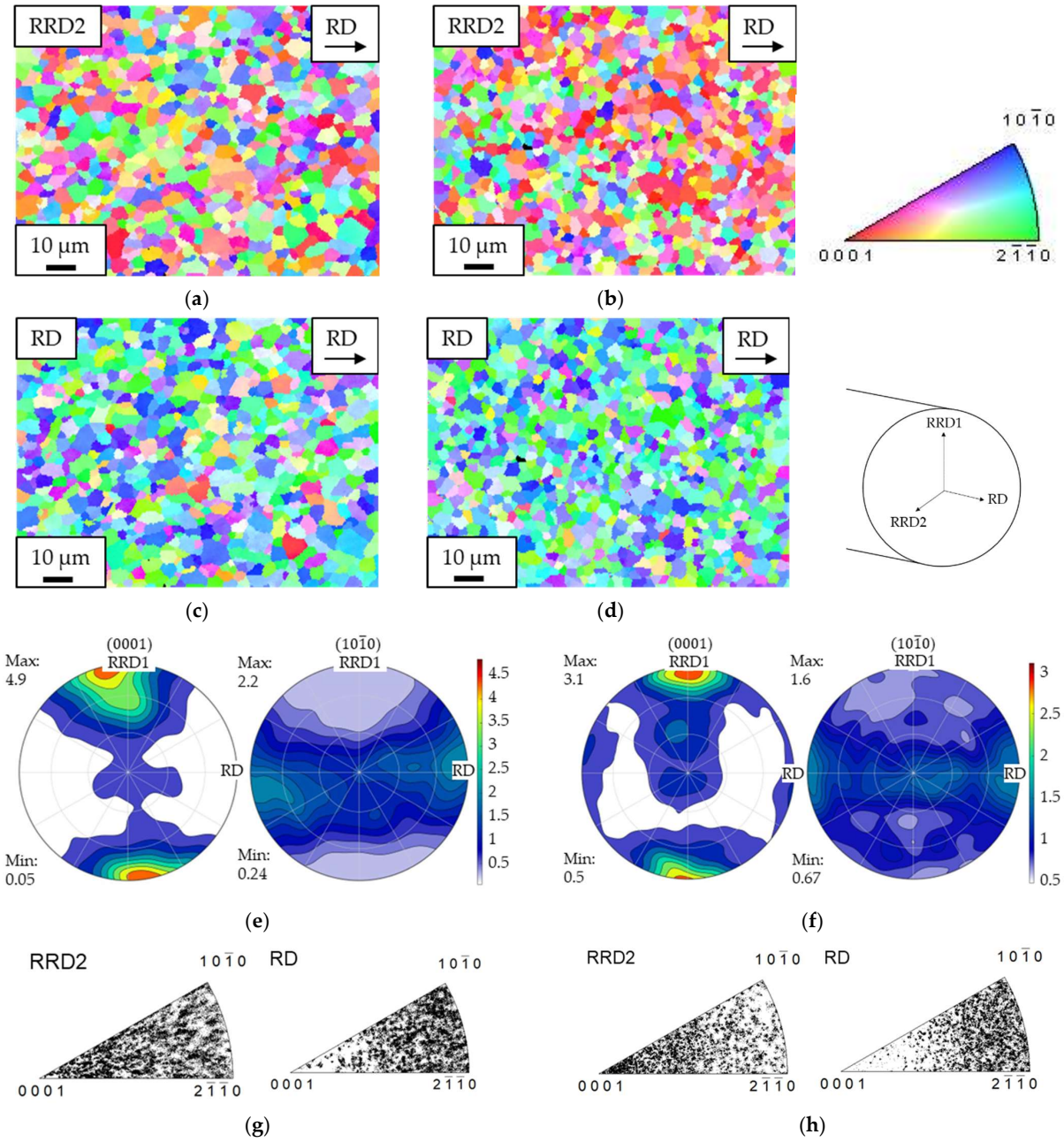

Figure 15. EBSD maps of the rolled magnesium alloy AZ31 transverse to rolling direction (RD) (**a**) in radial rolling direction 2 (RRD2), (**c**) in RD, and AZ91 transverse to RD (**b**) in RRD2 and (**d**) in RD. Pole figures of the rolled magnesium alloys (**e**) AZ31 and (**f**) AZ91. Inverse pole figures of (**g**) AZ31 and (**h**) AZ91 magnesium alloy.

Table 4 shows the hardness values of AZ31 and AZ91 in the heat-treated and rolled state. After hot rolling, a significant hardness increase is present for both alloys. On the one hand, the hardness increase is attributed to grain refinement because of dynamical recrystallization with increasing rolling pass, see Figure 16. On the other hand, the Al content (solid solution strengthening) influences hardness, as the values of the AZ91 alloy were significantly higher than the values of the AZ31 magnesium alloy.

Table 4. Hardness values of the magnesium alloys AZ31 and AZ91 in the heat-treated and rolled state.

Hardness HV10	Heat-Treated	Rolled
AZ31	46 ± 2	68 ± 2
AZ91	61 ± 2	92 ± 1

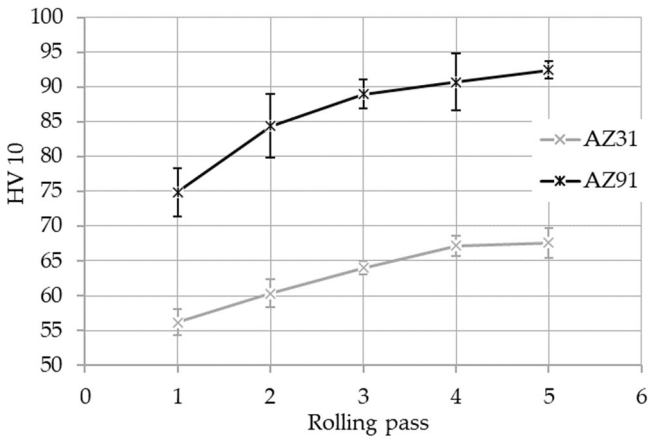

Figure 16. Hardness increases of AZ31 and AZ91 during rolling.

Table 5 shows the mechanical properties of the alloys AZ31 and AZ91 after five passes of hot rolling. An increase in strength and ductility is present for both alloys compared to the heat-treated state (cf. Table 3). Furthermore, the standard deviations could be reduced in the case of yield and tensile strength. This might be due to a reduction in grain size and refinement of the material. AZ31 still exhibits improved ductility, while AZ91 shows higher strengths. This is attributed to the lower, respectively, higher Al content, which leads to a higher SFE in AZ31 and, resp., solid solution strengthening in AZ91 [35,36].

Table 5. Mechanical properties of the alloys AZ31 and AZ91 in the rolled state.

Mechanical Properties	Yield Strength (MPa)	Tensile Strength (Mpa)	Elongation at Break (%)
AZ31	208 ± 3	283 ± 6	14 ± 0
AZ91	310 ± 1	384 ± 7	9 ± 2

Within the rolled state, the same DRX mechanisms were observed in both alloys as described in Section 3.2. Though the initial grain size differed, nearly the same mean grain size was obtained in both alloys after five passes of rolling. AZ31 and AZ91 exhibited a rolling texture after five passes of rolling. However, the texture intensity was lower for AZ91. The mechanical properties, as well as the hardness, could be improved by wire rolling. As in the heat-treated state, AZ31 exhibited a higher ductility while AZ91 exhibited higher strengths.

After five passes of hot rolling, which corresponds to a large strain, and a corresponding microstructure formation during DRX, the inheritance effect of a fine initial grain size is no longer evident, as it was in the heat-treated state. An initial grain size influences how

the DRX is initiated. The increased Al content, which influenced a fine initial grain size in AZ91 compared to AZ31, not only affects the initiation of DRX but also contributes to the final properties via solid solution strengthening and precipitation.

4. Conclusions

This study showed that a higher Al content causes a larger constitutional supercooling in the magnesium melt, which leads to a finer grain size in AZ91 compared to AZ31. Then, it investigated whether the alloying element influences the texture, DRX mechanisms, and mechanical properties during annealing and hot deformation. This study can be summarized as follows:

- In the cast state, the globular structure of the AZ31 alloy differs from the fully developed dendritic microstructure of the AZ91 alloy. This can be explained by the higher Al content, which promotes the formation of dendrites. After heat treatment, a globular grain structure is visible for both alloys. The grain size of the AZ91 alloy is lower compared to AZ31 after casting due to the higher Al content and its impact on constitutional supercooling. No preferred orientation is present for both alloys in the cast or heat-treated state. The hardness is increased in AZ91 compared to AZ31 due to the higher amount of Al and the solid solution strengthening effect. At room temperature, AZ91 exhibits higher strength due to the solid solution strengthening of the higher Al content, while AZ31 shows a higher elongation at the break due to its higher SFE.
- The solidification rate of both alloys shows a similar course but is also affected by the Al content. The calculated solidification rate of AZ91 was about 9.3 K/s, which is comparable to a typical solidification rate in the literature.
- The warm flow curves of the AZ91 alloy exhibit a steeper slope and decline compared to the AZ31 alloy. This is mainly due to the strengthening effect of the solute. Further, the maximum flow stresses of the AZ91 alloy are shifted to lower logarithmic strains and higher flow stresses compared to the AZ31 alloy. According to the flow curves, dynamic recrystallization (DRX) is probably more dominant than dynamic recovery. The calculated activation energy for DRX was 140 kJ/mol for AZ31 and 147 kJ/mol for AZ91. The start of the DRX for AZ91 is shifted to lower logarithmic strains compared to AZ31. It is, therefore, expected to see a higher amount of DRX grains in AZ91. The main DRX mechanisms are TDRX and DDRX in both alloys. It was detected that $Mg_{17}Al_{12}$ precipitates at the grain boundaries in AZ91, which influences the grain size through pinning (PSN).
- The same results on the DRX mechanisms were obtained in rolling tests, where a higher deformation rate was present. After five passes of rolling, a fine DRX grain size is present in both alloys. The wire rolling texture intensity in AZ91 is lower compared to AZ31. This is attributed to more randomly oriented grains that are present in AZ91 due to the precipitation of the secondary phase. Within five passes of rolling, the hardness can be increased in both alloys. Although AZ31 exhibits higher ductility in the rolled state, AZ91 shows higher strength values. This is probably due to the lower, respectively, higher Al content, which leads to a higher SFE in AZ31 and, resp., solid solution strengthening in AZ91.
- Due to a microstructure formation during DRX, the inheritance effect of a fine initial grain size is no longer evident, as it was in the heat-treated state. The increased Al content in AZ91 compared to AZ31 influences not only a fine grain size in the initial state but also the initiation of the DRX and final properties via solid solution strengthening and the precipitation of the secondary phase.

Author Contributions: Conceptualization, M.M.; methodology, M.M.; formal analysis, M.M.; investigation, M.M.; data curation, M.M.; writing—original draft preparation, M.M.; writing—review and editing, M.U. and U.P.; supervision, M.U. and U.P.; project administration, M.U. All authors have read and agreed to the published version of the manuscript.

Funding: This research received no external funding.

Data Availability Statement: The data presented in this study are available on request from the corresponding author. The data are not publicly available due to ongoing research.

Acknowledgments: We would like to acknowledge Jonas Lachmann's support regarding the SEM investigations (Institute of Material Science, TU Bergakademie Freiberg).

Conflicts of Interest: The authors declare no conflict of interest.

References

1. Siengchin, S. A review on lightweight materials for defence applications: Present and future developments. *Def. Technol.* **2023**, *24*, 1–17. [CrossRef]
2. Jayasathyakawin, S.; Ravichandran, M.; Baskar, N.; Anand Chairman, C.; Balasundaram, R. Mechanical properties and applications of Magnesium alloy—Review. *Mater. Today Proc.* **2020**, *27*, 909–913. [CrossRef]
3. Elambharathi, B.; Kumar, S.D.; Dhanoop, V.U.; Dinakar, S.; Rajumar, S.; Sharma, S.; Kumar, V.; Li, C.; Eldin, E.M.T.; Wojciechowski, S. Novel insights on different treatment of magnesium alloys: A critical review. *Heliyon* **2022**, *8*, e11712. [CrossRef]
4. Schichtel, G. *Magnesium Taschenbuch*; VEB Verlag Technik: Berlin, Germany, 1954.
5. Dahle, A.K.; Lee, Y.C.; Nave, M.D.; Schaffer, P.L.; StJohn, D.H. Development of the as-cast microstructure on magnesium-aluminium alloys. *J. Light Met.* **2001**, *1*, 61–72. [CrossRef]
6. Długosz, P.; Bochniak, W.; Ostachowski, P.; Molak, R.; Duarte Guigou, M.; Hebda, M. The Influence of Conventional or KOBO Extrusion Process on the Properties of AZ91 (MgAl9Zn1) Alloy. *Materials* **2021**, *14*, 6543. [CrossRef]
7. Kang, J.-H.; Park, J.; Song, K.; Oh, C.-S.; Shchyglo, O.; Steinbach, I. Microstructure analyses and phase-field simulation of partially divorced eutectic solidification in hypoeutectic Mg-Al Alloys. *J. Magnes. Alloys* **2022**, *10*, 1672–1679. [CrossRef]
8. Lee, Y.C.; Dahle, A.K.; StJohn, D.H. The Role of Solute in Grain Refinement of Magnesium. *Metall. Mater. Trans. A* **2000**, *31*, 2895–2906. [CrossRef]
9. Shen, M.J.; Wang, X.J.; Li, C.D.; Zhang, M.F.; Hu, X.S.; Zheng, M.Y.; Wu, K. Effect of submicron size SiC particles on microstructure and mechanical properties of AZ31B magnesium matrix composites. *Mater. Des.* **2014**, *54*, 436–442. [CrossRef]
10. Wang, X.; Liu, W.; Hu, X.; Wu, K. Microstructural modification and strength enhancement by SiC nanoparticles in AZ31 magnesium alloy during hot rolling. *Mater. Sci. Eng. A* **2018**, *715*, 49–61. [CrossRef]
11. Xu, Q.; Li, Y.; Ding, H.; Ma, A.; Jiang, J.; Chen, G.; Chen, Y. Microstructure and mechanical properties of SiCp/AZ91 composites processed by a combined processing method of equal channel angular pressing and rolling. *J. Mater. Res. Technol.* **2021**, *15*, 5244–5251. [CrossRef]
12. You, Z.; Jiang, A.; Duan, Z.; Qiao, G.; Gao, J.; Guo, L. Effect of heat treatment on microstructure and properties of semi-solid squeeze casting AZ91D. *China Foundry* **2020**, *17*, 219–226. [CrossRef]
13. Lee, D.H.; Lee, G.M.; Park, S.H. Difference in extrusion temperature dependences of microstructure and mechanical properties between extruded AZ61 and AZ91 alloys. *J. Magnes. Alloys* **2023**, *11*, 1683–1696. [CrossRef]
14. Ebrahimi, G.R.; Maldar, A.R.; Ebrahimi, R.; Davoodi, A. Effect of thermomechanical parameters on dynamically recrystallized grain size of AZ91 magnesium alloy. *J. Alloys Compd.* **2011**, *509*, 2703–2708. [CrossRef]
15. Gottstein, G. *Physikalische Grundlagen der Materialkunde*, 3rd ed.; Springer: Berlin/Heidelberg, Germany, 2007; ISBN 978-3-540-71104-9.
16. Mirzadeh, H. Grain refinement of magnesium alloys by dynamic recrystallization (DRX): A review. *J. Mater. Res. Technol.* **2023**, *25*, 7050–7077. [CrossRef]
17. Ghandehari Ferdowsi, M.R.; Mazinani, M.; Ebrahimi, G.R. Effects of hot rolling and inter-stage annealing on the microstructure and texture evolution in a partially homogenized AZ91 magnesium alloy. *Mater. Sci. Eng. A* **2014**, *606*, 214–227. [CrossRef]
18. Ebrahimi, M.; Wang, Q.; Attarilar, S. A comprehensive review of magnesium-based alloys and composites processed by cyclic extrusion compression and the related techniques. *Prog. Mater. Sci.* **2023**, *131*, 101016. [CrossRef]
19. Prakash, P.; Wells, M.A.; Williams, B.W. Hot deformation of cast AZ31 and AZ80 magnesium alloys—Influence of Al content on microstructure and texture development. *J. Alloys Compd.* **2022**, *897*, 1–11. [CrossRef]
20. Sitdikov, O.; Kaibyshev, R. Dynamic Recrystallization in Pure Magnesium. *Mater. Trans.* **2001**, *42*, 1928–1937. [CrossRef]
21. Xu, S.W.; Kamado, S.; Matsumoto, N.; Honma, T.; Kojima, Y. Recrystallization mechanism of as-cast AZ91 magnesium alloy during hot compressive deformation. *Mater. Sci. Eng. A* **2009**, *527*, 52–60. [CrossRef]
22. Guo, F.; Zhang, D.; Wu, H.; Jiang, L.; Pan, F. The role of Al content on deformation behavior and related texture evolution during hot rolling of Mg-Al-Zn alloys. *J. Alloys Compd.* **2017**, *695*, 396–403. [CrossRef]
23. Tahreen, N.; Chen, D.L.; Nouri, M.; Li, D.Y. Influence of aluminum content on twinning and texture development of cast Mg–Al–Zn alloy during compression. *J. Alloys Compd.* **2015**, *623*, 15–23. [CrossRef]

24. Li, X.; Jiao, F.; Al-Samman, T.; Ghosh Chowdhury, S. Influence of second-phase precipitates on the texture evolution of Mg–Al–Zn alloys during hot deformation. *Scr. Mater.* **2012**, *66*, 159–162. [CrossRef]
25. Robson, J.D.; Henry, D.T.; Davis, B. Particle effects on recrystallization in magnesium–manganese alloys: Particle-stimulated nucleation. *Acta Mater.* **2009**, *57*, 2739–2747. [CrossRef]
26. Jin, Z.-Z.; Cheng, X.-M.; Zha, M.; Rong, J.; Zhang, H.; Wang, J.-G.; Wang, C.; Li, Z.-G.; Wang, H.-Y. Effects of Mg17Al12 second phase particles on twinning-induced recrystallization behavior in Mg−Al−Zn alloys during gradient hot rolling. *J. Mater. Sci. Technol.* **2019**, *35*, 2017–2026. [CrossRef]
27. Zhu, H.; Yu, B.; Cai, J.; Bian, J.; Zheng, L. Effect of initial microstructures on microstructures and properties of extruded AZ31 alloy. *Mater. Sci. Technol.* **2023**, *39*, 1579–1591. [CrossRef]
28. Prakash, P.; Uramowski, J.; Wells, M.A.; Williams, B.W. Influence of Initial Microstructure on the Hot Deformation Behavior of AZ80 Magnesium Alloy. *J. Mater. Eng. Perform* **2023**, *32*, 2647–2660. [CrossRef]
29. *DIN EN 12438:2017*; Magnesium and Magnesium Alloys—Magnesium Alloys for Casting Anodes. Beuth Verlag: Berlin, Germany, 2017.
30. *ASTM B93/B93M-21*; Specification for Magnesium Alloys in Ingot Form for Sand Castings, Permanent Mold Castings, and Die Castings. ASTM International: West Conshohocken, PA, USA, 2021.
31. Bachmann, F.; Hielscher, R.; Schaeben, H. Texture Analysis with MTEX—Free and Open Source Software Toolbox. *SSP* **2010**, *160*, 63–68. [CrossRef]
32. *DIN EN 50125:2022*; Testing of Metallic Materials - Tensile Test Pieces. Beuth Verlag: Berlin, Germany, 2022.
33. Krbetschek, C.; Berge, F.; Oswald, M.; Ullmann, M.; Kawalla, R. Microstructure investigations of inverse segregations in twin-roll cast AZ31 strips. In *Magnesium Technology*; Springer: Cham, Switzerland, 2016; pp. 369–374. [CrossRef]
34. Pawar, S.; Zhou, X.; Hashimoto, T.; Thompson, G.E.; Scamans, G.; Fan, Z. Investigation of the microstructure and the influence of iron on the formation of Al8Mn5 particles in twin roll cast AZ31 magnesium alloy. *J. Alloys Compd.* **2015**, *628*, 195–198. [CrossRef]
35. Cáceres, C.; Rovera, D. Solid solution strengthening in concentrated Mg–Al alloys. *J. Light Met.* **2001**, *1*, 151–156. [CrossRef]
36. Muzyk, M.; Pakiela, Z.; Kurzydlowski, K.J. Generalized stacking fault energy in magnesium alloys: Density functional theory calculations. *Scr. Mater.* **2012**, *66*, 219–222. [CrossRef]
37. Park, S.S.; Lee, J.G.; Lee, H.C.; Kim, N.J. Development of wrought Mg alloys via strip casting. In *Essential Readings in Magnesium Technology*; Mathaudhu, S.N., Luo, A.A., Neelameggham, N.R., Nyberg, E.A., Sillekens, W.H., Eds.; Springer International Publishing: Cham, Switzerland, 2004; pp. 233–238.
38. Luo, A.A.; Fu, P.; Zheng, X.; Peng, L.; Hu, B.; Sachdev, A.K. Microstructure and Mechanical Properties of Die Cast Magnesium-Aluminium-Tin Alloys. *Magnes. Technol.* **2013**, *2016*, 341–345.
39. Fatemi-Varzaneh, S.M.; Zarei-Hanzaki, A.; Beladi, H. Dynamic recrystallization in AZ31 magnesium alloy. *Mater. Sci. Eng. A* **2007**, *456*, 52–57. [CrossRef]
40. Kim, K.; Ji, Y.; Kim, K.; Park, M. Effect of Al Concentration on Basal Texture Formation Behavior of AZ-Series Magnesium Alloys during High-Temperature Deformation. *Materials* **2023**, *16*, 2380. [CrossRef] [PubMed]
41. Pilehva, F.; Zarei-Hanzaki, A.; Fatemi-Varzaneh, S.M. The influence of initial microstructure and temperature on the deformation behavior of AZ91 magnesium alloy. *Mater. Des.* **2012**, *42*, 411–417. [CrossRef]
42. Yang, X.Y.; Sanada, M.; Miura, H.; Sakai, T. Effect of Initial Grain Size on Deformation Behavior and Dynamic Recrystallization of Magnesium Alloy AZ31. *MSF* **2005**, *488-489*, 223–226. [CrossRef]
43. Barnett, M.R.; Keshavarz, Z.; Beer, A.G.; Ma, X. Non-Schmid behaviour during secondary twinning in a polycrystalline magnesium alloy. *Acta Mater.* **2008**, *56*, 5–15. [CrossRef]
44. Lin, B.; Zhang, H.; Meng, Y.; Wang, L.; Fan, J.; Zhang, S.; Roven, H.J. Deformation behavior, microstructure evolution, and dynamic recrystallization mechanism of an AZ31 Mg alloy under high-throughput gradient thermal compression. *Mater. Sci. Eng. A* **2022**, *847*, 143338. [CrossRef]
45. Ullmann, M. Rekristallisationsverhalten von Geglühtem AZ31-Gießwalzband beim Warmwalzen. Ph.D. Thesis, TU Bergakademie Freiberg, Freiberg, Germany, 2014.
46. Poletti, C.; Dieringa, H.; Warchomicka, F. Local deformation and processing maps of as-cast AZ31 alloy. *Mater. Sci. Eng. A* **2009**, *516*, 138–147. [CrossRef]
47. Wang, T.; Nie, K.; Deng, K.; Liang, W. Analysis of hot deformation behavior and microstructure evolution of as-cast SiC nanoparticles reinforced magnesium matrix composite. *J. Mater. Res.* **2016**, *31*, 3437–3447. [CrossRef]
48. Arndt, F.; Berndorf, S.; Moses, M.; Ullmann, M.; Prahl, U. Microstructure and Hot Deformation Behaviour of Twin-Roll Cast AZ31 Magnesium Wire. *Crystals* **2022**, *12*, 173. [CrossRef]
49. Sherby, O.D.; Taleff, E.M. Influence of grain size, solute atoms and second-phase particles on creep behavior of polycrystalline solids. *Mater. Sci. Eng. A* **2002**, *322*, 89–99. [CrossRef]
50. Peng, W.P.; Li, P.J.; Zeng, P.; Lei, L.P. Hot deformation behavior and microstructure evolution of twin-roll-cast Mg–2.9Al–0.9Zn alloy: A study with processing map. *Mater. Sci. Eng. A* **2008**, *494*, 173–178. [CrossRef]

51. Liu, Z.; Xing, S.; Bao, P.; Li, N.; Yao, S.; Zhang, M. Characteristics of hot tensile deformation and microstructure evolution of twin-roll cast AZ31B magnesium alloys. *Trans. Nonferrous Met. Soc. China* **2010**, *20*, 776–782. [CrossRef]
52. Xu, S.W.; Matsumoto, N.; Kamado, S.; Honma, T.; Kojima, Y. Effect of Mg17Al12 precipitates on the microstructural changes and mechanical properties of hot compressed AZ91 magnesium alloy. *Mater. Sci. Eng. A* **2009**, *523*, 47–52. [CrossRef]